PERGAMON International Journal of Mechanical Sciences 43 (2001) 2237–2260

International Journal of MECHANICAL SCIENCES

www.elsevier.com/locate/ijmecsci

Molecular dynamics (MD) simulation of uniaxial tension of some single-crystal cubic metals at nanolevel

R. Komanduri[a,*], N. Chandrasekaran[a], L.M. Raff[b]

[a] *Mechanical and Aerospace Engineering, Oklahoma State University, 218 Engineering North, Stillwater, OK 74078-5016, USA*

[b] *Chemistry Department, Oklahoma State University, Physical Sciences I, Stillwater, OK 74078-5016, USA*

Received 5 April 2000; received in revised form 14 February 2001

Abstract

Molecular Dynamics (MD) simulations of uniaxial tension at nanolevel have been carried out at a constant rate of loading (500 m s^{-1}) on some single-crystal cubic metals, both FCC (Al, Cu, and Ni) and BCC (Fe, Cr, and W) to investigate the nature of deformation and fracture. Failure of the workmaterials due to void formation, their coalescence into nanocracks, and subsequent fracture or separation were observed similar to their behavior at macroscale. The engineering stress–strain diagrams obtained by the MD simulations of the tensile specimens of various materials show a rapid increase in stress up to a maximum followed by a gradual drop to zero when the specimen fails by ductile fracture. The radius of the neck is found to increase with an increase in the deformation of the specimen and to decrease as the ductility of the material decreases. In this investigation, the strain to fracture is observed to be lower with the BCC materials than FCC materials. In the case of BCC crystals, no distinct linear trend in the engineering stress–strain characteristics is observed. Instead, rapid fluctuations in the force values were observed. If the drop in the force curves can be attributed to the rearrangement of atoms to a new or modified crystalline structure, it appears that BCC materials undergo a significant change in their structure and subsequent realignment relative to the FCC materials, as previously reported in the literature. While good correlation is found between the D- and α-parameters of the Morse potential with the ultimate strength and the strain to failure for the FCC metals, no such correlation is found for the BCC metals. From this, it appears that Morse potentials may not represent the deformation behavior of BCC metals as accurately as FCC metals and alternate potentials may need to be considered.

Keywords: Tension; Molecular dynamics simulation; Nano-mechanical properties

* Corresponding author. Tel.: +1-405-744-5900; fax: +1-405-744-7873.
E-mail address: ranga@ceat.okstate.edu (R. Komanduri).

0020-7403/01/$ - see front matter
PII: S0020-7403(01)00043-1

1. Introduction

Technological advancements have paved the way toward the development of micro- and nano-components in micro-electro-mechanical systems (MEMS) and micro-opto-electro-mechanical systems (MOEMS) [1]. The micro- and nano-structural elements used in them are required to withstand the complex stress state with minimal probability of failure. At the same time, the structural elements made of these materials are produced by such special processes that they are almost devoid of defects. These ideal materials (with no or very few defects and strength close to their theoretical values) are going to be the norm rather than exception for nanocomponents in MEMS and MOEMS. Hence, an investigation of the strength and deformation behavior of defect-free materials at nanometer level greatly facilitates the analysis of nano-components.

Generally, the material properties of the nano-components are determined using nanoindentation tests with extremely light loads in the range of nano-Newtons [2]. While tensile tests are most common in determining the mechanical properties at macrolevel, such tests at nanoscale are extremely difficult, if not impossible to conduct. Even if this is possible, the costs involved in performing nano-regime tensile testing would be significant due to the inherent complexity of the equipment. Also, the production of defect-free materials in the form of tensile specimens would be very difficult. An alternative approach is MD simulations. Even though the fracture stress of real crystals are dependent on their defect density, the theoretical strength of ideal materials depend on the way defect-free crystals would deform and fail [3].

In this investigation, MD simulations of tension are carried out to study the behavior of a range of single crystal cubic metals, both FCC (Al, Cu, and Ni) and BCC (Fe, Cr, and W) under uniaxial loading. An attempt is made to relate the mechanical properties and deformation behavior determined by the simulation with the Morse potential parameters (D and α-parameters) used in the modeling of these materials.

2. Literature review

In view of the vast amount of literature in the general field of MD simulation, only literature relevant to MD simulations of tensile testing will be briefly reviewed. Macmillan and Kelley [4] conducted MD simulations of uniaxial tension on NaCl crystals using a simple, two-body, central force Born–Mayer potential. Marked anisotropy in the ideal tensile strength, with a pronounced minimum for the $\langle 1\,0\,0\rangle$ plane was found. This is consistent with the observed cleavage on this plane. Also, the maximum strain the crystal can withstand before failure depended on the direction of the applied strain and whether the unit cell dimensions perpendicular to the stress direction are allowed to relax or not. Parinello and Rahman [5] introduced a new Lagrangian formulation to perform MD simulations on systems under external stress. Using this method, they applied uniaxial stress to a FCC cubic lattice (Ni) with periodic boundary conditions at 350 K. Under uniaxial compression, they suggested a transformation in the crystal structure from FCC to HCP. The maximum tensile strength under uniaxial tension was reported to be 11×10^{10} dyn cm^{-2}.

Selinger et al. [6] investigated the statistical thermodynamics of stretched 2-D Lennard–Jones type perfect crystals. They reported an increase in stress to a critical value after which the crystal became unstable and failed. The failure was attributed to the growth of defects caused by thermal fluctuations. It was suggested that a change to the stable state due to the thermal fluctuations is possible only when the applied stress is very close to the critical stress value. Selinger et al. [7] investigated the failure of a 3-D FCC (Pt) metal using a hybrid MD/Monte Carlo computational technique that allowed changes in both shape and volume of the periodic boundary condition. Under low temperature and slow loading conditions, a crystal–crystal phase transition was reported to precede crystal failure. As the stretching force was increased, they observed the extension to increase steadily followed by a sudden jump to a longer extension. The crystal was then reported to stretch continuously in a steady manner until it broke. The authors attribute the sudden jump to a phase change undergone by the crystal as a result of the imposed stress. The phase change was reported to take place in order to enable the crystal to partially relieve the imposed stress. At higher temperatures, direct failure of the system due to stress-induced melting was reported.

Lynden-Bell [8,9] conducted MD/Monte Carlo simulations of uniaxial tension at various temperatures [$(0.04-0.7)T_m$, where T_m is the bulk melting temperature of the material] on platinum, gold, rhodium, and silver. Failure of the crystals was reported to be due to void formation and their growth to nanocracks. At low temperatures the stress was reported to increase to a maximum after which a series of structural rearrangements of the crystal accompanied by a decrease in the stress magnitude was reported. Highly ductile metals, such as platinum/gold were reported to develop local regions of disorder first, in comparison to slip between planes of atoms relative to each other, with not-so-ductile metals, such as rhodium or silver. At temperatures above half the melting point, all the metals were reported to be disordered before failure by void formation. A liquid-like, highly disordered region was said to exist in the fracture region. This occurs when the free energies of the ordered and disordered states are equal. It appears that an investigation of the tensile behavior at various temperatures would require consideration of both short range as well as long range order in the material. Thus, the potential function used should incorporate many-body terms to represent the behavior of the metal in bulk.

Rentsch and Inasaki [10] conducted MD simulations of uniaxial tension of silicon to verify the material representation of silicon in fracture. They reported a linear increase in the stress–strain relation followed by a sudden break down to zero. They also reported anisotropic deformation of silicon. The Young's modulus and the specific surface energy of silicon were found to be 171 GPa and 0.393 J m^{-2}, respectively.

Doyama [11] conducted MD simulations of tension on iron and copper single crystals with free boundaries. The iron and copper specimens were prepared with a notch and pulled in the [1 1 1] and [0 0 1] directions, respectively. They suggest that the notch is normally a source of dislocations due to stress concentration and the dislocations are mostly half-dislocations. They observed no perfect dislocations in their simulations. With decreasing notch thickness, the effect of the crack was reported to decrease although interaction still exists across the notch. The initial stage of deformation was found to be due to dislocations followed by cross linkage between dislocations on different slip planes in the middle stage resulting in work hardening with the final stage consisting of many dislocations and inhomogenous deformation. Studies of

crack propagation, dynamic instability, and subsequent failure by MD simulations of tension have been reported by other researchers [12–14].

Kitamura et al. [15] conducted atomic simulations of tension on a nanoscopic wire, film, and bulk of a Ni lattice without defects. To investigate the effect of constraint of transverse deformation on the fracture process, simulations for the bulk were conducted under two conditions: (1) free transverse stress condition and (2) fully constrained condition. During the fracture process, the wire and the film were reported to exhibit multiple slip resulting in the neck formation after a strain of 1.0. Concentrated shear deformation with the localization of slip in the necked region was reported to result in ductile fracture. However, with the bulk specimen, they reported absence of necking by slip even at a strain of 1.0. The transformation was reported to be induced by the tensile strain. In the case of tension experiments with free transverse stress condition, i.e. without the constraint of transverse deformation, yielding was reported to be brought about by the crystallographic slip on the (1 1 1) planes at a strain of $\sim$0.1. The yield stress in tension was found to be $\sim$15–20 GPa and very little difference in strength was reported between the wire, the film, and the bulk. Multiple slip even after yielding of the crystal and significant plastic deformation were reported to cause ductile shear fracture. In the simulations with constraint of transverse deformation, the yield stress was reported to reach 40 GPa. No plastic strain was generated. This is attributed to the restriction of dislocation glide. Cleavage cracks were observed and found to bring about brittle fracture and hence a change in the fracture mode.

Heino et al. [16] conducted MD simulations of tension and shear on Cu for [1 0 0] [0 1 0], [0 1 $\bar{1}$][0 1 1], and [$\bar{1}$ $\bar{1}$ 2][1 1 1] orientations. The differences between the calculated and the experimental tensile and shear moduli were reported to be in the range of 2–6% and 3–15%, respectively. This difference was attributed to the effect of boundary conditions. With a free boundary condition, plastic deformation by slip on the {1 1 1} planes was reported. An increase in the strength with decreasing system size and a decrease with increasing disorder were also found. The computed failure strain was 8.5%. In the study of crack propagation, generation of microvoids and crack propagation as a result of coalescing of microvoids was observed.

Heino et al. [17] studied MD simulations of tensile loading (periodic as well as free boundaries) on copper with various types of defects, namely, point defects, grain boundaries, and initial void serving as a crack seed. They used a many-atom, ab initio type potential obtained from effective medium theory [18]. The internal temperature of the system was controlled with a Nose′–Hoover thermostat that was in contact with the boundaries but not with the process region. The boundary between these regions was assumed to be smooth. With periodic grain boundaries, the tensile modulus of copper in the elastic region was reported to be 210 GPa. They concluded that the simulation results are in quantitative agreement with the experiments. They obtained the tensile modulus of the grain boundary to be $\sim$40% less than the whole system. They also stated that the modulus of the grain boundary depend crucially on its microstructure. Cracking was reported to have been initiated at a location where the strain concentration due to differences in the modulus of the grain boundary and the ordered bulk was the largest. After initiation, the crack was reported to propagate along the grain boundaries. The strength of the system with periodic boundaries was reported to be $\sim$10.3 GPa. In the tensile loading of a system with grain boundaries but with free boundaries, they reported absence of crack propagation

with failure occurring due to grain boundary sliding. In this case, the system was reported to fail at low strain and stress values.

3. Methodology of molecular dynamics (MD) simulation

Fig. 1(a) is a schematic of a conventional tensile specimen and Fig. 1(b) is a schematic of the gage section used in the MD simulations for different work-materials showing various regions of interest. The motion of the atoms in the moving zone are determined by direct integration of the classical Hamiltonian equations of motion using a fourth-order Runge–Kutta method. The motions of the peripheral atoms are calculated from the same solution but modified by the presence of velocity reset functions after Riley et al. [19] associated with each atom in the peripheral zone. Heat dissipation is carried out through the peripheral atoms to simulate thermal contact with a heat bath at 293 K. The boundary atoms are fixed in position and serve to reduce the edge effects and maintain proper symmetry of the lattice. Further details are given in Chandrasekaran et al. [20].

The potential used in this investigation is a pairwise sum of Morse potentials of the form [21]

$$V = \sum_{i,j} \Phi(r_{ij}), \tag{1}$$

where

$$\Phi(r_{ij}) = D[\exp\{-2\alpha(r_{ij} - r_o)\} - 2\exp\{-\alpha(r_{ij} - r_o)\}]. \tag{2}$$

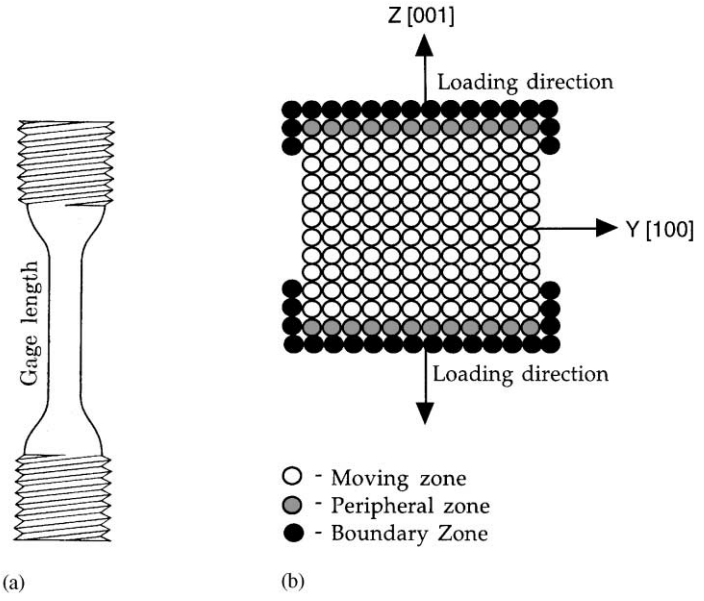

Fig. 1. Schematic of (a) conventional tensile specimen and (b) the gage section used in the MD simulations, respectively, for different work-materials showing various regions of interest.

Table 1
Computational parameters used in the MD simulation of uniaxial tensile loading

Configuration	3-D
Potential used	Morse potential
Workmaterial dimensions	$5a \times 15a \times 15a$, a—lattice constant
Tensile loading condition	Uniaxial
Speed of simulation	500 m/s
Bulk temperature	293 K

The Morse potential parameters for the tensile specimen, namely, D, α and r_e are generally adjusted to the measured sublimation enthalphy, Debye temperature, and nearest-neighbor spacings. The cutoff radius (r_c) is chosen such that the ratio of the potential at the cutoff point to that at equilibrium is less than 4%. The use of such a cutoff radius ensures that the calculations will not consume large amounts of computational time in evaluating the forces that are near zero. The MD simulations require the solution of $6N$ (N-total number of atoms) simultaneous, coupled, first-order differential equations of motion. This solution is obtained using a fourth-order Runge–Kutta algorithm with a fixed integration step size of 1.019×10^{-15} s. Integration accuracy is monitored using back-integration and energy conservation requirements with the velocity reset procedure turned off.

The specimen used for the gage section is a nanofilm of $5a \times 15a \times 15a$ long, where a is the lattice constant. The total number of atoms used in the simulations ranges from 2250 to 4500 depending on the crystal structure. A Digital alpha workstation (Model 500) with a clock speed of 500 MHz was used for the simulation. The rate of loading was rather high ($500\ \mathrm{m\ s^{-1}}$) to keep the computational time to a reasonable value. The free surfaces (i.e., front and back surfaces as well as the sides of the specimen) are free from any external loads, as in conventional tensile testing. The top and bottom sides are fixed by the boundary atoms. The regions above the top and below the bottom of the boundary atoms represent the material above and below the gage section [Fig. 1(a)], respectively, similar to a conventional tensile specimen where deformation is minimal and mostly elastic. The crystal was set-up with a cubic orientation and the uniaxial tensile force was applied along the [0 0 1] direction. Table 1 gives the dimensions of the workmaterial, rate of loading, bulk temperature, etc. Initially, the structure of the specimen was setup, then relaxed to the equilibrium position using a damped trajectory procedure [22] after which the tensile load was applied. The MD simulations were carried out till separation occurs in the tensile specimen.

4. Results and discussion

4.1. On the nature of deformation and fracture under tensile loading

The MD simulation plots of the gage sections of the tensile specimens at various stages of uniaxial loading are shown in Figs. 2(a) to (f)–7(a) to (f). Figs. 2–4 are for the FCC materials, Al,

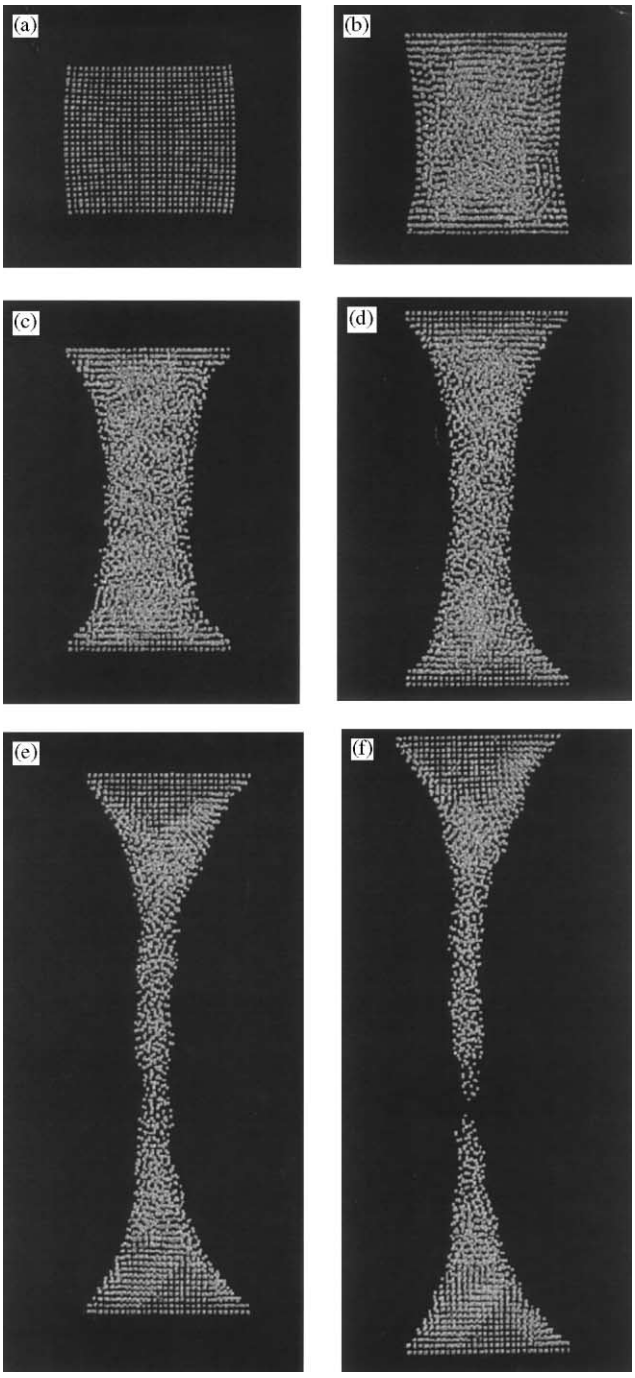

Fig. 2(a)–(f). MD simulation plots of the gage section of a tensile specimen at various stages of uniaxial loading for Al.

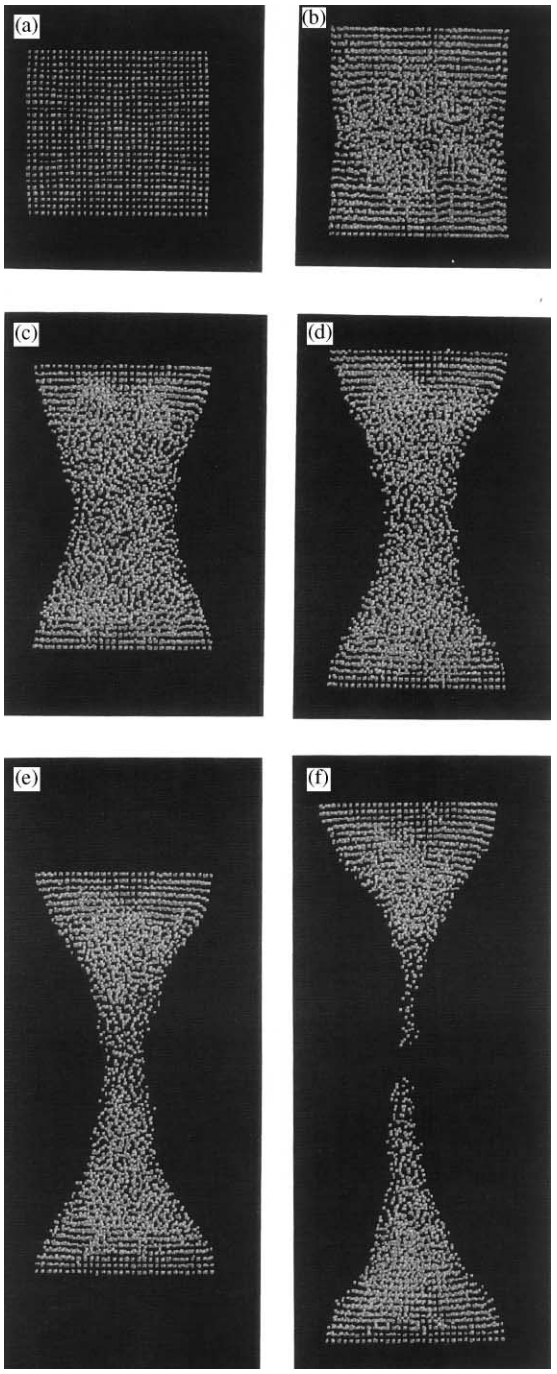

Fig. 3(a)–(f). MD simulation plots of the gage section of a tensile specimen at various stages of uniaxial loading for Cu.

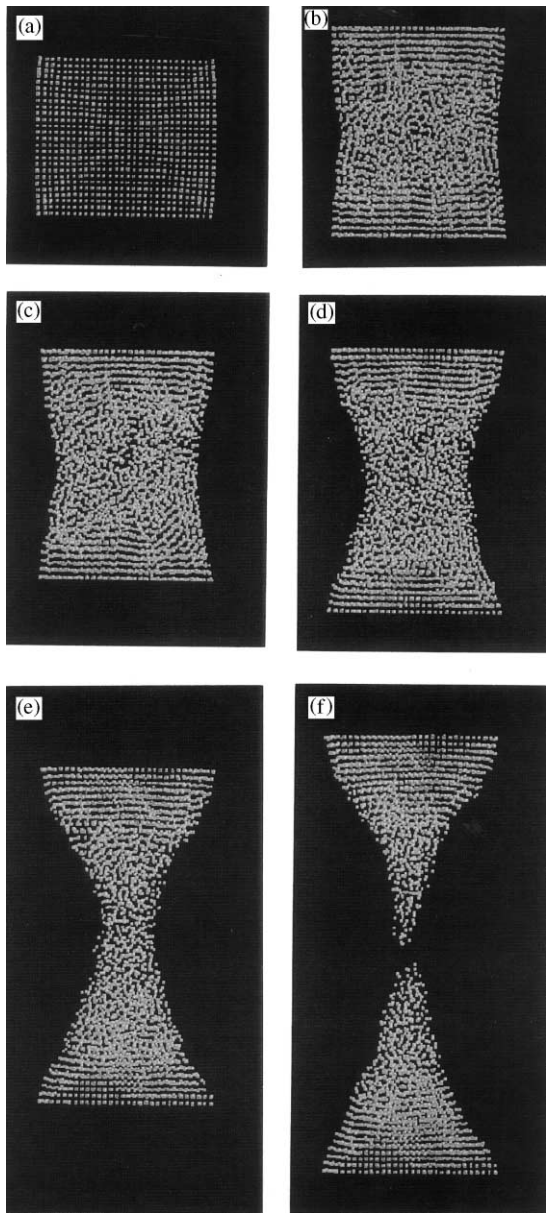

Fig. 4(a)–(f). MD simulation plots of the gage section of a tensile specimen at various stages of uniaxial loading for Ni.

Cu, and Ni, respectively, and Figs. 5–7 are for the BCC materials, Fe, Cr, and W, respectively. It may be noted that the discussion of the results presented here is based not only on the MD simulation plots of the various stages presented here but also on the detailed study of the animation of the process which was accomplished using a special computer program developed for this purpose [23].

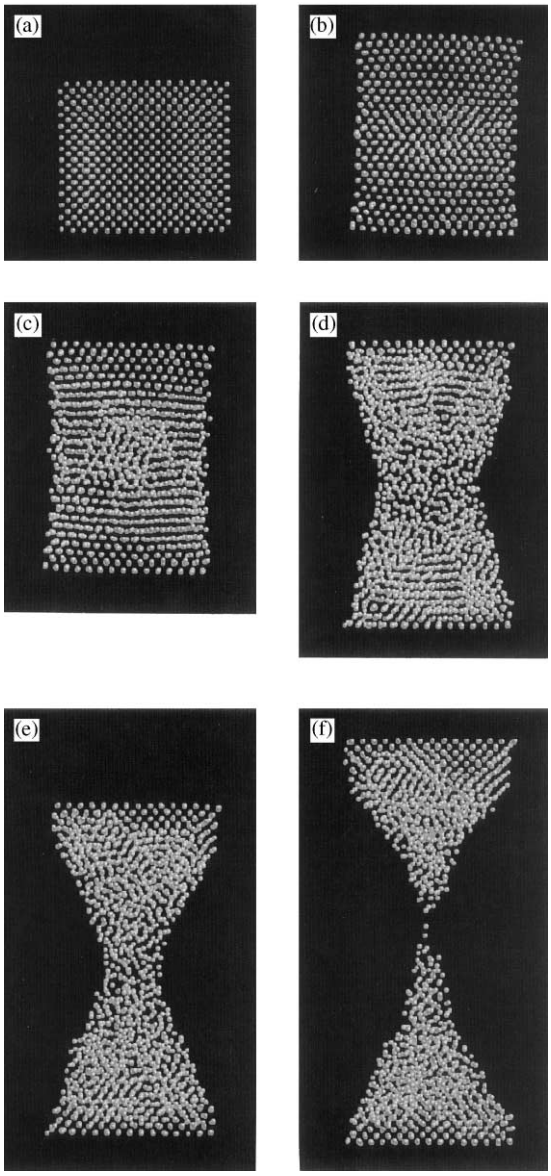

Fig. 5(a)–(f). MD simulation plots of the gage section of a tensile specimen at various stages of uniaxial loading for Fe.

For the FCC materials after relaxation, the specimens were found to be slightly compressed due to internal forces. Fig. 2(a) shows a small compressive bulge of the specimen after the relaxation for the case of Al. A similar situation is found for the case of the other two FCC metals investigated, namely, Cu and Ni. This, however, was not the case with the BCC materials [compare Figs. 5(a), 6(a), and 7(a) with Figs. 2(a), 3(a), and 4(a)]. Considerable disorder in the gage section of the crystal was observed during the early stages of loading for all FCC metals [see (b) and (c) of Figs. 2–4]. As the workmaterial was extended, bridging of the top

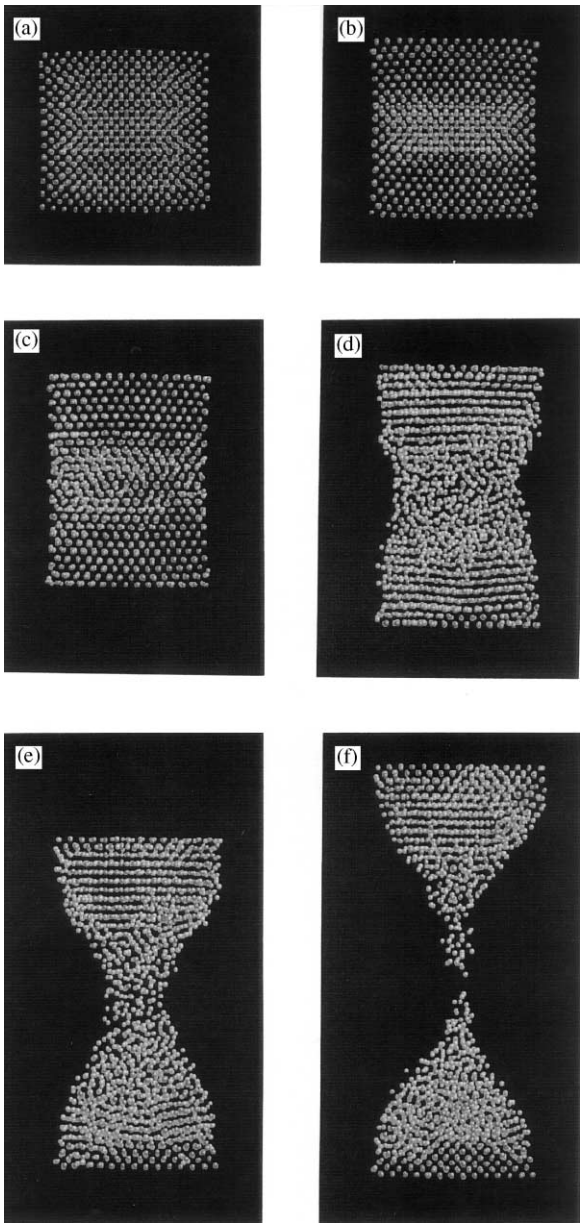

Fig. 6(a)–(f). MD simulation plots of the gage section of a tensile specimen at various stages of uniaxial loading for Cr.

and bottom portions of the crystal by a disordered neck of constantly decreasing diameter can be seen [(c)–(e) of Figs. 2–4]. Since Al is a highly ductile material, the atoms hold together under larger strain before the voids formed during the early stages of deformation coalesce and form a ductile fracture. Towards the later stages, the neck is elongated almost linearly to a very large strain [Fig. 2(f)]. On subsequent pulling, the necked region [Fig. 2(f)] separates

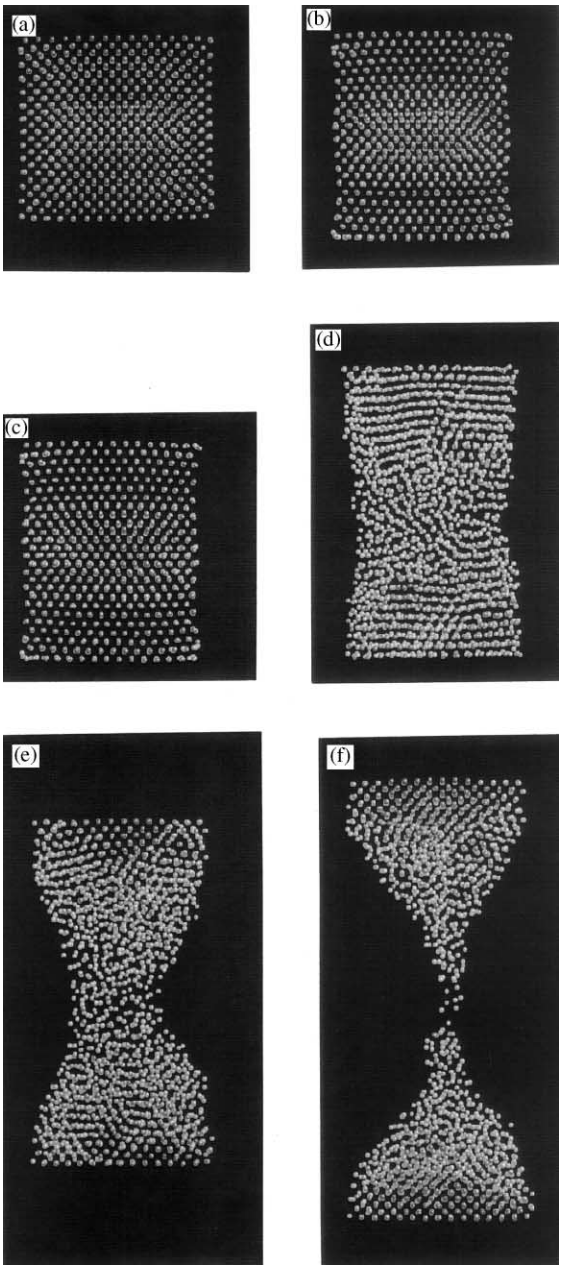

Fig. 7(a)–(f). MD simulation plots of the gage section of a tensile specimen at various stages of uniaxial loading for W.

culminating in the failure. The radius of the neck was found to increase with increase in the deformation of the specimen and to decrease with decrease in the ductility of the material. Thus, the radius decreases monotonically as we go from Al to Cu to Ni. The region of disordered material as well as the extent of void formation were also found to decrease with decrease in

the ductility of the material. Initially, dislocations at $\sim 45^{\circ}$ were observed in the animation for the case of Cu and Ni but due to the high disorder, further dislocation propagation was difficult to observe.

In the case of BCC materials, a different behavior was observed during the early stages. As can be seen from Figs. 5(a), 6(a), and 7(a), the workmaterials seem to be in an excited state during the initial stage (i.e. after one time step). This localized disorder develops a weak region in the specimens which results in subsequent necking. In the case of Fe, the layers above and below the necked region are arranged perpendicular to the loading direction with significant void volume fraction in the necked region [Figs. 5(c) and (d)]. The observed crystal order [Fig. 5(c)] is different from the initial crystal set-up [Fig. 5(a)]. On subsequent loading, the crystal order above and below the necked region disappears and the localized disorder spreads throughout the entire length of the workmaterial [Figs. 5(d) and (e)].

In the case of Cr, the disorder observed in the workmaterial during the initial step [Fig. 6(a)] disappears on further loading [Fig. 6(b)]. However, a localized disorder develops in the center of the workmaterial [Fig. 6(b)] as observed with iron [Fig. 5(b)]. Similar to Fe, the regions above and below the weak region (mid-plane) are arranged perpendicular to the loading direction. The new crystal arrangement causes generation of voids in the weak region [Figs. 6(c) and (d)]. Subsequent elongation of the Cr crystal results in fracture [Fig. 6(f)].

In the case of tungsten, as loading progresses, the disorder [Figs. 7(a) and (b)] disappears and the crystal assumes a new orientation [Fig. 7(c)]. Even though, the disorder still exists around the mid-plane of the crystal, it is minimal in comparison to Fe and Cr. Due to complete reorientation of the crystal and a definite order in the atomic positions, the disorder on subsequent elongation seems to concentrate around the mid-plane of the crystal [Fig. 7(d)]. Significant void fraction can be observed in the necked region. Once again, the layers above and below the necked region are arranged perpendicular to the loading direction [Figs. 7(d) and (e)]. Since the defects are highly concentrated in the necked region, subsequent loading results in early failure of tungsten [Fig. 7(f)].

Based on the animations, as well as the MD simulations at various stages of deformation (Figs. 2–7), the strain to fracture was observed to be lower with the BCC materials compared to the FCC materials. This can be observed by comparing Figs. 2(f)–7(f) which shows a pictorial view of the variations in the strain to fracture of various crystals. Al behaves like a very ductile material extending significantly [Figs. 2(e) and (f)]. The amount of extension decreases as one moves from Al to Cu [Fig. 3(f)], to Ni [Fig. 4(f)], to Fe [Fig. 5(f)], and Cr [Fig. 6(f)] with W exhibiting minimum strain before fracture [Fig. 7(f)]. Also, the radius and length of the neck was observed to be different for different materials [Figs. 2(e)–7(e)]. In the case of FCC materials, the workmaterial was disordered from the early stages of necking till the end. Consequently, it was not possible to observe any structural changes in the crystal. The disorder was observed to extend throughout the entire length of the workmaterial. The void volume fraction was distributed throughout the specimen with FCC materials while in the case of BCC materials, they were concentrated around the necked region. Consequently, FCC materials were able to withstand higher strain before failure. In the case of BCC materials, the atoms tend to rearrange with their neighbors to form a different or modified crystal structure. The workmaterial above and below the necked region was observed to arrange itself perpendicular

to the loading direction. The crystal symmetry in these regions resulted in a weak mid-plane with higher void volume fraction. Consequently, the crystal failed around this region at a lower strain in comparison to the FCC materials. This constant rearrangement of the atoms with the BCC materials will be shown to result in significant force variations. It will be shown, based on the force trends, that structural transformations also occur with FCC materials, albeit to a lesser extent in comparison to BCC materials.

4.2. On the nature of force variation under tensile loading

Figs. 8(a)–(f) show the engineering stress–strain diagrams obtained by MD simulation of the tensile specimens of Al, Cu, Ni (FCC) [Figs. 8(a)–(c)] and Fe, Cr, and W (BCC) [Figs. 8(d)–(f)], respectively. They show a rapid increase in stress up to the maximum tensile strength of the specimen under consideration followed by a gradual drop to zero when the specimen fails by ductile fracture. In the case of FCC materials, especially Al and Ni [Figs. 8(a) and (c)], the forces start below the zero point prior to the application of the tensile loading. It was pointed out in Section 4.1 that after the relaxation procedure, the FCC specimens were under slight compression [Figs. 2(a), 3(a), and 3(c)] due to internal stresses. This compression causes the initial forces to be negative. The slope of the linearly increasing curve is more apparent in the case of FCC materials with Ni exhibiting the maximum slope [Fig. 8(c)] followed by Cu [Fig. 8(b)] and Al [Fig. 8(a)], as can be expected from the known ductility of these materials. Unlike in conventional tensile testing, where the stress–strain diagram is essentially smooth with a linear slope in the elastic region, in nano tensile testing, a series of steps of rise and fall in the stress values with engineering strain occurs in the initial elastic region. This is followed by a plastic region up to the maximum stress. This behavior can be attributed to strain hardening and subsequent softening of the material due to dislocation pileup and subsequent rapid motion of the dislocations. Animation of the tensile tests indicated considerable reorganization of the atoms followed by rapid movement due to the generation of dislocations. Also, no clear demarcation of linear elastic range nor the yield point is visible. It is, therefore, difficult to calculate exact values of the elastic moduli or the elastic constants with any degree of certainty. The general practice is to obtain the modulus for small values of strain from a second degree polynomial that was fitted to the stress–strain diagram [16].

In the case of BCC materials no distinct linear trend in the engineering stress–strain characteristics is observed [Figs. 8(d)–(f)]. The diagrams show a number of sudden jumps of rise and fall in the stress values. Cr shows a significant drop and rise after reaching a maximum tensile strength point followed by an increase to the global maximum tensile strength point before dropping down to zero [Fig. 8(e)]. Such high force drops are also observed with Fe [Fig. 8(d)] and W [Fig. 8(f)]. In the case of Fe, Cr, and W [Fig. 8(d)–(f)], the fluctuations in the force curves during the early stages can be compared with the structural changes seen in the MD simulations, as have been discussed earlier. If the drop in the force curves can be attributed to the rearrangement of atoms to a new crystal structure, it appears that BCC materials undergo significant changes in their structure and subsequent realignment in comparison to FCC materials.

Lynden-Bell [9] suggested that the position of the maximum stress is the point of failure of the material and marks the change from reversible to irreversible behavior. Actually, reversible

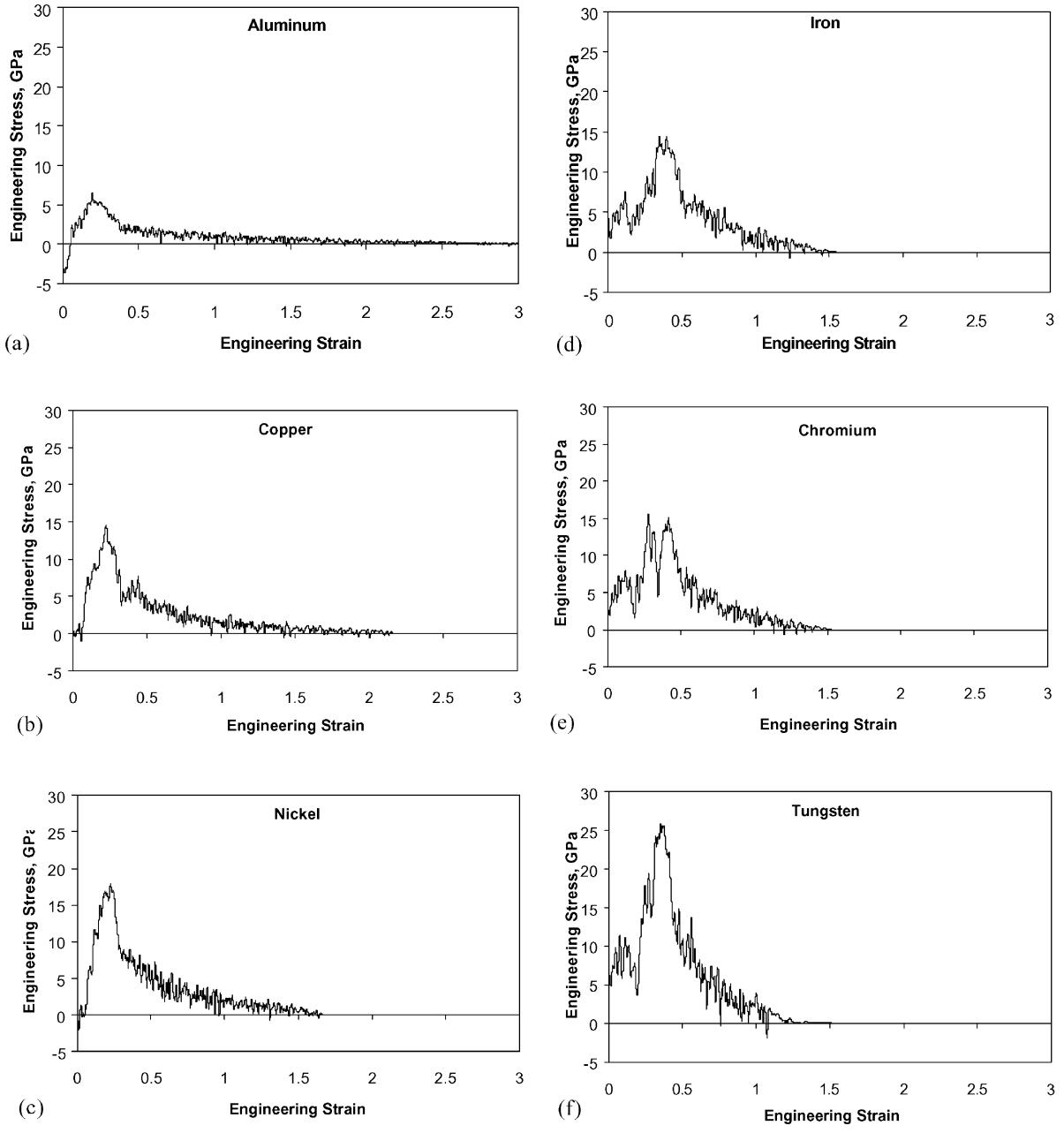

Fig. 8. Engineering stress–strain diagrams obtained by MD simulation of the tensile specimens of various materials, namely, Al, Cu, Ni (FCC) [(a)–(c)] and Fe, Cr, and W (BCC) [(d)–(f)], respectively.

behavior stops after the elastic limit and once the yield point is reached. This is far below the position of maximum stress (or the ultimate stress). In the MD simulations conducted here, we observed that in the case of FCC workmaterials, even before the maximum stress point

Table 2
Results of MD simulation of uniaxial tensile loading with various materials

Material	Ultimate strength (GPa)	Strain at max. stress (nm/nm)	Strain to failure (nm/nm)
Aluminium	13.02	0.20	3.19
Copper	28.63	0.22	2.17
Nickel	36.04	0.23	1.67
Iron	28.85	0.40	1.52
Chromium	31.10	0.28	1.52
Tungsten	51.14	0.34	1.40

is reached the crystal has undergone significant amount of irreversible deformation as would be expected. The fluctuations in the force curves observed for both the FCC and BCC workmaterials [Figs. 8(a)–(f)] suggest the irreversibility of the process even before the maximum stress point is reached. If one considers the structural transformations and the subsequent drop in the force to be due to plastic deformation in the crystal, then it is no longer a reversible process.

Table 2 gives the measured (from MD simulation) tensile strength and strain to fracture of the various materials used in this study. As can be expected, W exhibits the highest strength (ultimate strength of ~51 GPa) while Al exhibits the lowest strength (ultimate strength of ~13 GPa). The strength of Ni was estimated to be ~36 GPa which is close to the value (40 GPa) reported by Kitamura et al. [15]. The strength of Cu was estimated to be ~28 GPa. Heino et al. [17] reported a strength of 10.3 GPa for polycrystalline Cu. Since our simulations were performed on defect-free single crystals, the estimated strength of copper should be much higher than that reported by Heino et al. [17]. The strength can be expected to decrease with increasing disorder in the workmaterial as reported by Heino et al. [17]. The strain to fracture can also be observed to be different for the various materials used in this investigation. Tungsten showed an earlier fracture at ~1.4 while in the case of aluminium the maximum strain before fracture is ~3.2. The BCC materials studied in this investigation exhibited higher stress accommodation in comparison to the FCC materials (Table 2). This can be attributed to the higher degree of structural transformations observed with the BCC materials compared to the FCC materials.

4.3. *Effect of Morse potential parameters* (D *and* α) *on deformation and fracture*

Table 3 gives the Morse potential parameters (D and α) of the various materials (both FCC and BCC) used in this investigation after Girifalco and Weizer [24]. Figs. 9(a) and (b) show the variation of force with the interatomic distance for various values of D (with α and r_o fixed) and α-parameters (with D and r_o fixed), respectively. The fixed values of the D- and α-parameters in Figs. 9(a) and (b) are that of copper. As the atoms are pulled apart during uniaxial tension, the forces between them transform from a short range repulsive to medium range attractive, subsequently, reaching an equilibrium position. Further separation (long range) leads to zero force. As the D-parameter increases, the magnitude of the force required to separate

Table 3
Morse potential parameters used in MD simulation of uniaxial tensile loading [24]

Material	Crystal structure	Dissociation energy, D (eV)	Equilibrium radius, r_o (Å)	α-parameter ($Å^{-1}$)	Lattice constant (Å)
Aluminium	FCC	0.2703	3.253	1.1650	4.05
Copper	FCC	0.3429	2.866	1.3590	3.62
Nickel	FCC	0.4205	2.780	1.4199	3.52
Iron	BCC	0.4172	2.845	1.3890	2.87
Chromium	BCC	0.4414	2.754	1.5721	2.89
Tungsten	BCC	0.9906	3.032	1.4116	3.17

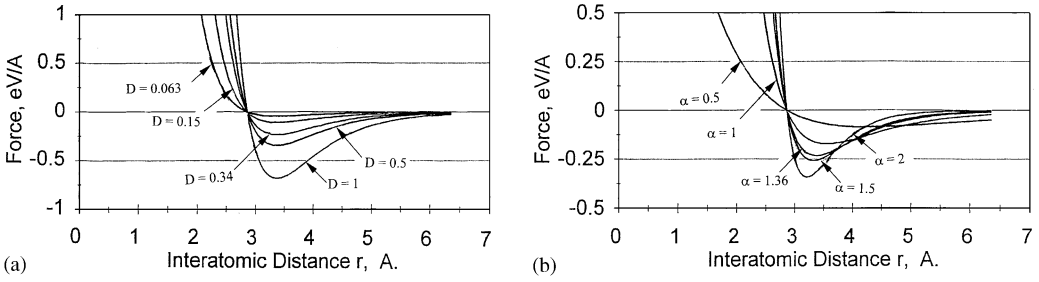

Fig. 9. Variation of force with the interatomic distance for various values of D-(with α and r_o fixed) and α-parameters (with D and r_o fixed) used in the Morse potential, respectively.

the atoms increases. As the α-parameter increases, the long range forces tend to approach zero at shorter interatomic distance, i.e., higher slope of the force with interatomic distance at shorter interatomic distance [Fig. 9(b)]. Consequently, a material with the lowest α-parameter would withstand maximum strain before failure as the long range forces approach zero at higher interatomic distance with decreasing α-parameter. Hence, the D-parameter and the α-parameter of the Morse potential can be used as an indication of the material strength and ductility. The lower the value of the D-parameter and the α-parameter, the more ductile the material is with lower strength and vice-versa.

Figs. 10(a) and (b) and Figs. 11(a) and (b) show the variation of the ultimate strength and the strain to failure with the D-parameter and the α-parameter, respectively. It can be seen that, as expected, the ultimate strength increases almost linearly for the FCC materials, namely, Al, followed by Cu, and Ni [Figs. 10(a) and 11(a)] with increase in the D-parameter and the α-parameter, respectively. In contrast, for the BCC metals, while there is an increase in the ultimate strength with increase in the D-parameter [Fig. 10(a)], this was not so with increase in the α-parameter [Fig. 11(a)]. Similarly, the strain to failure decreases almost linearly with increase in the D-parameter [Fig. 10(b)] and α-parameter [Fig. 11(b)], respectively, for the FCC materials, namely, Al, followed by Cu, and Ni as can be expected. However, for the BCC

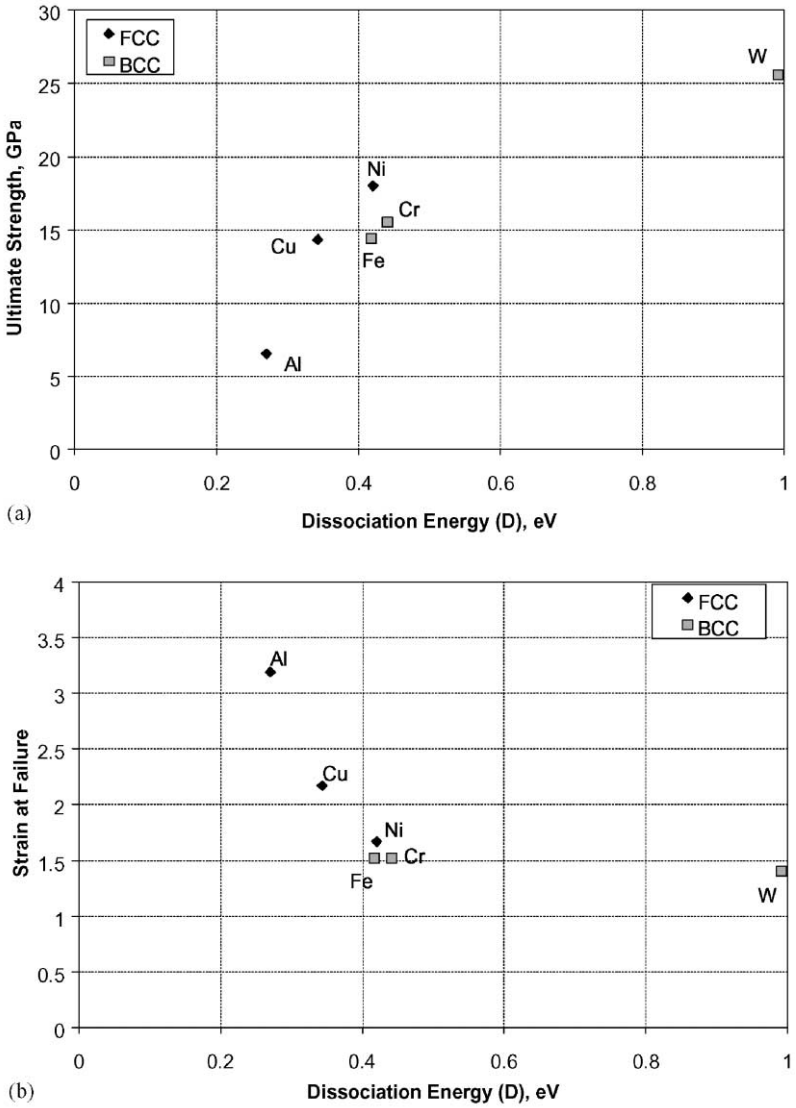

Fig. 10. Variation of (a) ultimate strength and (b) strain at fracture with dissociation energy (D), respectively.

metals the strain to fracture seems to be independent of both the D-parameter and the α-parameter [Figs. 10(b) and 11(b)]. For example, even though, the dissociation energy of the BCC work-materials used in this investigation varied from $\sim$0.4 to 1, the strain to failure remains nearly constant [Fig. 10(b)]. It can be seen from this that it is rather difficult to interpret the variation of D- and α-parameters on the strength and strain behavior of BCC metals. Such behavior suggests that a Morse potential may not represent the deformation behavior of the BCC metals as well as the FCC metals.

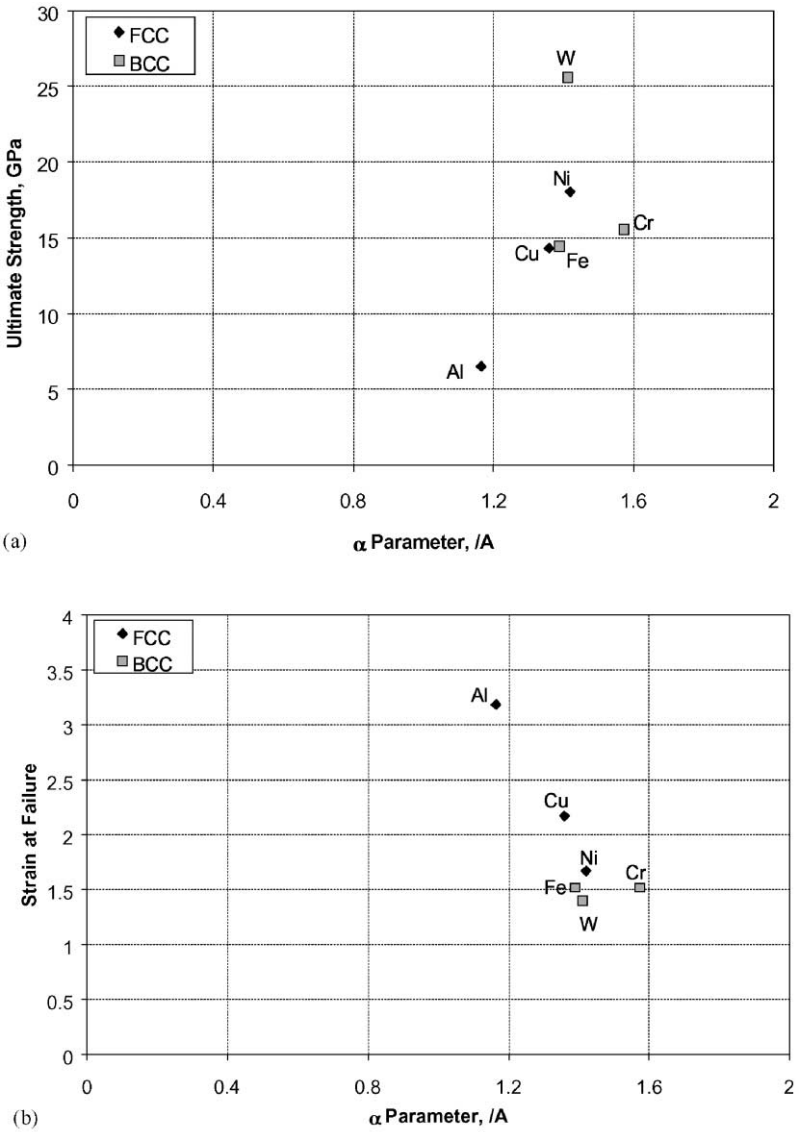

Fig. 11. Variation of (a) ultimate strength and (b) strain to failure with α-parameter, respectively.

4.4. *Effect of strain rate or rate of loading on the tensile response*

The MD simulations of uniaxial tension were conducted at three loading rates of 500, 250, and 100 m s^{-1}. This study was carried out specifically to investigate if the high stress–strain fluctuations observed with the BCC materials can be attributed to significant structural changes or due to an artifact at high loading rates (500 m s^{-1}) employed in the simulation. Simulations were performed for one BCC (Cr) and one FCC material (Ni) as representative of these materials.

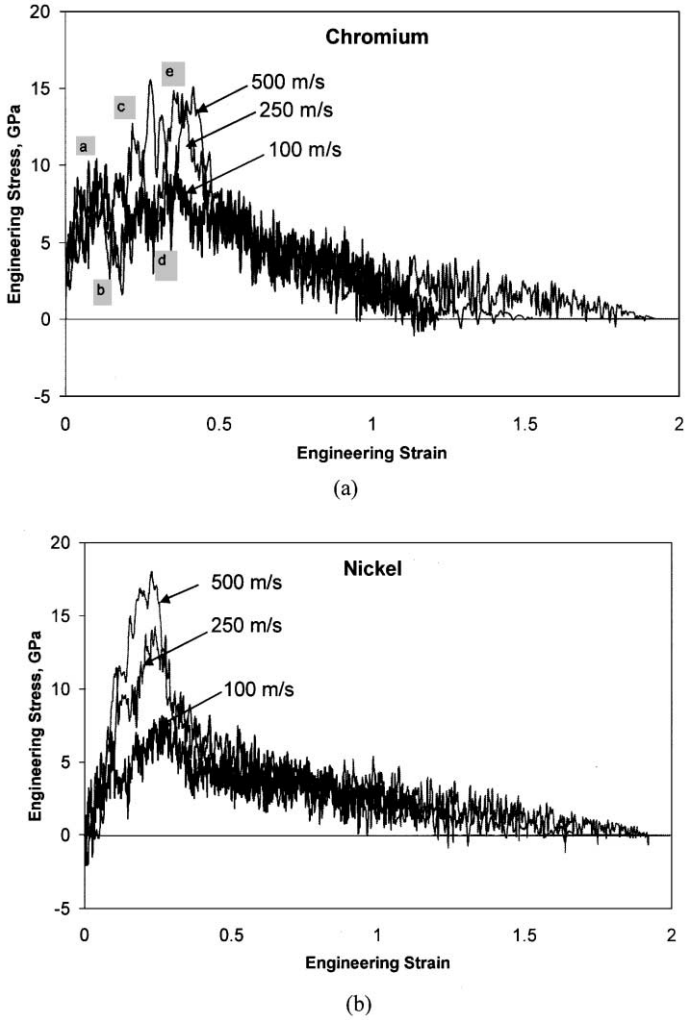

Fig. 12. Variation of the engineering stress with strain at different loading rates (500, 250, and 100 m s^{-1}) for: (a) a BCC (Cr); and (b) an FCC material (Ni), respectively.

Figs. 12(a) and (b) show the variation of engineering stress–strain distribution at different loading rates for Cr and Ni, respectively. Both, Cr [Fig. 12(a)] and Ni [Fig. 12(b)] show an initial decreasing slope with increasing strain. They also show a decrease in the ultimate stress with decreasing loading rate as supported by both theory and experimentation [25]. The stress–strain distribution during the initial and final stages of tension overlap, irrespective of the strain rate. The stress fluctuation also exhibits an increase in the frequency and a decrease in the amplitude with decreasing loading rate.

Fig. 12(a) shows that the high fluctuations in the stress–strain curve at 500 m s^{-1} [see Fig. 8(e)] repeat themselves even at lower strain rates. For example, at a strain rate of 250 m s^{-1}

for Cr, the stress fluctuates from point '*a*' through '*d*' finally reaches the maximum stress at '*e*' before the stress decreases to zero [Fig. 12(a)]. Similar fluctuations can also be observed with other strain rates, namely 100 and 500 m s^{-1}. However, the strain at which these high fluctuations are observed seem to vary with strain rate. Based on this result, it appears that the high fluctuations (higher amplitude) in the stress–strain curve for BCC materials are not due to the high loading rates but due to the significant structural transformations observed with BCC materials in comparison to FCC materials, as explained earlier.

In the case of Ni, a gradual and systematic drop in the ultimate tensile strength with decreasing strain rate is observed [Fig. 12(b)]. The ultimate tensile strength of Ni decreases by a factor of $\sim$3 while the ultimate strength of Cr decreases by a factor < 2 as the strain rate is reduced by a factor of five. However, according to theory [25], one would expect BCC metals to exhibit higher strain rate sensitivity than FCC metals. The strain at which the ultimate strength is measured seems to remain constant for both BCC and FCC metals. However, the strain to failure increases with decreasing strain rate for Ni while it does not follow a particular trend with Cr. These contradictions again suggest that Morse-type potentials may not adequately represent BCC metals.

5. Conclusions

1. MD simulations of uniaxial tension have been carried out at constant rate of loading (500 m s^{-1}) on some single-crystal cubic metals, both FCC (Al, Cu, and Ni) and BCC (Fe, Cr, and W) to investigate the nature of deformation and fracture in these materials. Failure of the workmaterials due to void formation, their coalescence into nanocracks, and subsequent fracture or separation are observed to be similar to their behavior at macroscale.

2. For FCC materials, considerable disorder in the gage section of the crystal is observed during the early stages of loading. Further loading resulted in the disorder spreading through the entire length of the workmaterial. In the case of BCC materials, the disorder is observed to be highly localized around the midplane of the workmaterial. The layers above and below the necked region are arranged perpendicular to the loading direction. The new crystal arrangement generates voids in the weak region. Due to the differences in the defect distribution and crystal reorientation, the strain to fracture is observed to be lower with the BCC materials compared to the FCC materials.

3. The radius and length of the neck are observed to be different for different workmaterials. They increase with increase in the deformation of the specimen and decrease with decrease in the ductility of the material.

4. The engineering stress–strain diagrams obtained from the MD simulation of the tensile specimens show a rapid increase in stress up to the maximum followed by a gradual drop to zero when the specimen fails by ductile fracture. The slope of the linearly increasing curve is more prominent in the case of FCC materials than BCC materials. BCC materials exhibit a number of sudden fluctuations of the force values. If the drop in the force curves can be attributed to the rearrangement of atoms to a new crystal structure, then it appears that BCC materials undergo a significant change in their structure and subsequent realignment in comparison to the FCC materials, as previously reported in the literature.

5. Unlike conventional tensile testing, where the stress–strain diagram is essentially smooth with a linear slope in the elastic region, in nano tensile testing, a series of steps of fluctuations in the stress value with engineering strain in the initial elastic region followed by a plastic region up to the maximum value are found. These fluctuations can be attributed to the strain hardening and subsequent softening of the material due to dislocation pileup and subsequent rapid motion of the dislocations.

6. The measured tensile strength (from MD simulations) showed that W exhibits the highest strength (ultimate strength of ~51 GPa) while Al exhibits the lowest strength (ultimate strength of ~13 GPa). The ultimate strength of Cu, Ni, Fe, and Cr are evaluated to be ~28, 36, 29, and 31 GPa, respectively.

7. The strain to fracture was observed to be minimum with tungsten (~1.4), followed by iron and chromium (~1.52), nickel (~1.67), and copper (~2.17). Aluminium exhibited maximum ductility undergoing a maximum strain of ~3.2 before failure. It can thus be seen that strain values at nanolevels are significantly larger than similar values at macrolevel.

8. As expected, irreversible behavior during the loading/unloading process (for both FCC and BCC lattices) was observed even before the maximum stress point (ultimate tensile strength) was reached. This is expected as the yield point marks the demarcation between reversible and irreversible flow.

9. It appears that the D- and α-parameters of the Morse potential can be used as an indication of the material ductility and strength for FCC materials. The strength of the workmaterial decreases with decreasing D- and α-parameter while the strain to failure increases.

10. While good correlation was found between the D- and α-parameters of the Morse potential with the ultimate strength and the strain to failure for the FCC metals, no such correlation was found for the BCC metals. From this it appears that Morse potentials may not represent the deformation behavior of the BCC metals as accurately as the FCC metals and alternate potentials may need to be considered.

11. MD simulations of uniaxial tension at different loading rates (500, 250, and 100 m s^{-1}) for one BCC (Cr) and one FCC material (Ni) showed an initial decrease in slope with increasing strain and a decrease in the ultimate stress with decreasing loading rate as supported by both theory and experimentation [25]. Based on the simulation results for BCC materials at different loading rates, it appears that the high stress fluctuations in the stress–strain curve for BCC materials can be attributed not to the high loading rates, but to the significant structural transformations possible with BCC materials in comparison to FCC materials, as reported in the literature.

Acknowledgements

This project is sponsored by grants from the Manufacturing Processes and Machines Program (DMI-9523551) of the Division of the Design, Manufacture, and Industrial Innovation (DMII) and the Tribology and Surface Engineering Program (CMS-9414610) of the Division of Civil and Mechanical Structures of the National Science Foundation. The authors thank Drs. Kesh Narayanan (Acting DD), R. Rajurkar, and Delcie Durham of DMII, Dr. B.M. Kramer DD of Engineering Centers, and Dr. J. Larsen Basse of the Tribology and Surface Engineering Program

for their interest in and support of this work. One of the authors (R.K.) also thanks the A.H. Nelson, Jr Endowed Chair in Engineering for the financial support in the preparation of the manuscript. The authors also thank Dr. Ali Noori-Khajavi for his initial assistance with the simulation work and Mr. Robert Stewart with the animation.

References

[1] Bhushan B. Handbook of micro/nano tribology. New York: CRC Press, 1995.
[2] Pethica JB, Hutchings R, Oliver WC. Hardness measurements at penetration depths as small as 20 nm. Philosophical Magazine A 1983;48/4:593–606.
[3] Lynden-Bell RM. The fracture of perfect crystals under uniaxial tension at high temperatures. Journal of Physics: Condensation of Matter 1992;4:2172–38.
[4] Macmillan NH, Kelly A. The mechanical properties of perfect crystals. Proceedings of the Royal Society (London) A 1972;330:291–308.
[5] Parinello M, Rahman A. Polymorphic transitions in single crystals: a new molecular dynamics method. Journal of Applied Physics 1981;52(12):7182–90.
[6] Selinger RLB, Wang ZG, Gelbart WM. Statistical thermodynamic approach to fracture. Physical Review A 1991;43(8):4396–400.
[7] Selinger RLB, Lynden-Bell RM, Gelbart WM. Stress-induced failure and melting of ideal solids. Journal of Chemical Physics 1993;98(12):9808–18.
[8] Lynden-Bell RM. Computer simulations of fracture at the atomic level. Science 1994;263:1704–5.
[9] Lynden-Bell RM. A simulation study of induced disorder, failure and fracture of perfect metal crystals under uniaxial tension. Journal of Physics: Condensation of Matter 1995;7:4603–24.
[10] Rentsch R, Inasaki I. Investigation of surface integrity by molecular dynamics simulation. Annals of CIRP 1995;44(1):295–8.
[11] Doyama M. Simulation of plastic deformation of small iron and copper single crystals. Nuclear Instruments and Methods Physics Research B 1995:102–7.
[12] Sieradzki K, Dienes GJ, Paskin A, Massoumzadeh B. Atomistics of crack propagation. Acta Metallurgica 1988;36(3):651–63.
[13] Abraham FF, Brodbeck D, Rafey RA, Rudge WE. Instability dynamics of fracture: a computer simulation investigation. Physical Review Letters 1994;73(2):272–5.
[14] Zhou SJ, Beazley DM, Lomdahl PS, Holian BL. Large scale molecular dynamics simulations of three-dimensional ductile failure. Physical Review Letters 1997;78(3):479–82.
[15] Kitamura T, Yashiro K, Ohtani R. Atomic simulation on deformation and fracture of nano-single crystal of nickel in tension. JSME International A 1997;40(4):430–5.
[16] Heino P, Hakkinen H, Kaski K. Molecular-dynamics study of mechanical properties of copper. Europhysics Letters 1998;41(3):273–8.
[17] Heino P, Hakkinen H, Kaski K. Molecular-dynamics study of copper with defects under strain. Physical Review B 1998;58(2):641–52.
[18] Norskov JK, Lang ND. Effective medium theory of chemical binding: application to chemisorption. Physical Review B 1980;21:2131–6.
[19] Riley ME, Coltrin ME, Diestler DJ. A velocity reset method of simulating thermal motion and damping in gas–solid collisions. Journal of Chemical Physics 1988;88:5934–42.
[20] Chandrasekaran N, Noori-Khajavi A, Raff LM, Komanduri R. A new method for MD simulation of nanometric cutting. Philosophical Magazine B 1998;77(1):7–26.
[21] Morse PM. Diatomic molecules according to the wave mechanics. II vibrational levels. Physical Review 1929;34:57–64.
[22] Raff LM. Energy transfer in reaction dynamics of matrix-isolated 1,2-difluoroethane. Journal of Chemical Physics 1990;93:3160–76.

[23] Stewart R. Investigation on molecular dynamics simulation of nanometric cutting. M.S. Thesis, Oklahoma State University, Stillwater, OK, 1998.
[24] Girifalco LA, Weizer VG. Application of the Morse potential function to cubic metals. Physical Review 1959;114(3):687–90.
[25] Hertzberg RW. Deformation and fracture mechanics of engineering materials. 4th ed. New York: Wiley, 1996.